Effect of the boron element in a Li–P–S system

Audric Neveu, Hari Raj, Vincent Pelé, Christian Jordy, Valérie Pralong

ARTICLE

Effect of Boron Element in Li-P-S system

Audric Neveu [a,b], Hari Raj [a,b], Vincent Pelé [c], Christian Jordy [c], and Valerie Pralong [*, a,b]

Received 00th January 20xx,
Accepted 00th January 20xx

DOI: 10.1039/x0xx00000x

Lithium-ion batteries are nowadays a mature technology for the energy storage. However, some safety problems have been identified during the operation in high power applications such as fire incident in electric vehicles. The most promising solution to improve the safety of lithium-ion batteries is replacing current organic liquid based electrolyte with solid electrolyte. In this context, new solid electrolytes having chemical and electrochemical stability with high ionic conductivity needs to be discovered. Therefore, in the present study, a new LGPS-type structure domain is highlighted for the Li-B-P-S system. The ionic conductivity of prepared solid electrolytes in the Li-B-P-S system has been achieved upto 10^{-4} S/cm, and higher stability against lithium metal as compared to $Li_{10}GeP_2S_{12}$. These solid electrolytes also show better electrochemical characteristics in all solid-state batteries.

Introduction

Li-ion batteries represent a growing market with the development of electric vehicles. However, the conventional Li-ion batteries use a highly flammable non-aqueous liquid electrolyte that poses safety concerns[1]. Therefore, intensive research studies over the past 5 years have been focused on the development of all solid-state batteries, wherein solid electrolyte is a key component. Solid electrolytes must meet technological requirements such as high ionic conductivity, negligible electronic conductivity, wide voltage window stability (0-5 V), chemical compatibility with cathode and anode materials, and relatively simple fabrication at large scale and low cost[2].

In 2011, Kamaya et al.[3] discovered a new structure with the composition $Li_{10}GeP_2S_{12}$ (LGPS). This material exhibits a very high ionic conductivity of 12 mS/cm at ambient temperature due to specific structure of this compound, which forms channels of lithium along the c axis. However, this compound is expensive as it contains germanium and also instable at low potential due to reduction of Ge^{4+} to Ge^0 (metallic)[4]. Due to the high flexibility of the structure, germanium can be replaced by other elements of group 14 of the periodic table e.g. Si[5,6], Sn[7], or by aliovalent elements like Al[8]. In addition to replacing expensive Ge, structure malleability allows good control of the lithium concentration as these substitutions will induce cation vacancies.

However, substitution of the Ge also did not solve the problem of instability as stable interface could not be obtained with these elements, resulting in low coulombic efficiency in the cell [9]. One solution to improve stability issue could be use of none-metallic elements only in the composition, for example, the material $Li_{3.2}PS_4$ showed smallest irreversible capacity at the first cycle[10].

Another promising non-metallic element is boron which has shown positive impact on ionic conductivity. In the initial study as glass material, the mixture of Li_2S and B_2S_3 has shown ionic conductivity of 0.09 mS/cm at room temperature[11]. Glass with addition of other elements such as silicon, iodine or phosphorus was also tried and reported with increased ionic conductivity at room temperature. Till now, the maximum ionic conductivity at room temperature is reported 2.1 mS/cm by mixing Li_2S, B_2S_3, LiI and SiO_2 together[12]. The annealing of these precursors can be performed to obtain new materials. By mixing Li_2S and B_2S_3, a thio-lisicon material with BS_3^{3-} units instead of tetrahedral units is reported[13]. Recently, more complex structure such as $Li_{7.5}B_{10}S_{18}Cl_{1.5}$ was obtained from this system with good ionic conductivity[14].

In a previous study, synthesis of compounds from the binary Li_3PS_4-Li_3BS_3 was reported but the synthesis conditions were not described thoroughly[15]. The obtained compounds have shown Li_3PS_4 polymorph structure and reported ionic conductivity of 2.2×10^{-4} S/cm at ambient temperature for the best sample.

In the present study, by introducing the planetary milling step during the synthesis of the samples, we succeeded obtained an LGPS-type structure by substituting germanium with boron. Furthermore, the study reports a series of new solid electrolytes for all solid-state batteries.

Results and discussion

This study started with the discovery of an unidentified peak during the annealing of compositions in the Li_2S-P_2S_5-B_2S_3 system, suggesting the formation of new composite. As shown in the Figure S1 for the composition 0.6 Li_3PS_4 – 0.4 Li_3BS_3, if the mixture of Li_2S,

[a] Normandie Univ, Ensicaen, Unicaen, CNRS, Crismat, 14000 Caen, France.
[b] Réseau sur le Stockage Electrochimique de l'Énergie (RS2E), 80000 Amiens, France.
[c] SAFT, 111-113 Bd Alfred Daney 33074 Bordeaux, France.
† Dr. A. Neveu, Dr. H. Raj, Dr. C. Jordy, Dr. V. Pele, Dr. V. Pralong
Electronic Supplementary Information (ESI) available: [supplementary figures]. See DOI: 10.1039/x0xx00000x

P_2S_5 and B_2S_3 powders is annealed under 500°C, two phases β-Li_3PS_4 and Li_7PS_6 are found. However, at a higher temperature, some unidentified new peaks appear at 11.7°, 19.0°, 22.4°, 29.6° and 35.2°. Although, this system has been already studied previously by K. Homma et al.[15], and only γ and β-Li_3PS_4 phases were reported, but, there was no information given about the annealing process. Whereas, based on our study, we have observed that a high temperature annealing and a better mixing with the help of ball milling is necessary for obtaining the new structure. Furthermore, if temperature is further increased, peaks of β-Li_3PS_4 phase become sharper, suggesting an enhanced crystallization of β-Li_3PS_4 phase. In our study, the sample having lowest impurity was obtained at 550°C. To improve the composition of this phase, we further explored the pseudo-ternary system Li_2S-B_2S_3-P_2S_5.

Figure 1 represents the pseudo-ternary diagram Li_2S-B_2S_3-P_2S5, and large domain of stability of this phase has been highlighted during the exploration. The previously reported glass material synthesized by Zhang et al.[11,16] are also shown on the ternary diagram. These studies have been divided in three binaries. The first represented binary diagram by green dashed line with filled triangle is (1-x) Li_3PS_4- x Li_3BS_3 (0<x<0.5). We were inspired by the approach of Kanno et al.[17] for the discovery of the LGPS compound in the Li_3PS_4-Li_4GeS_4 binary system. Then, we enlarged the exploration of compositions outside this binary, which are represented by blue and purple dashed lines with square symbols. All the studied compositions are given in Table 1. In our study, it can be noticed that we are working with a higher concentration of lithium as compared to Zhang's studies along with a higher boron content.

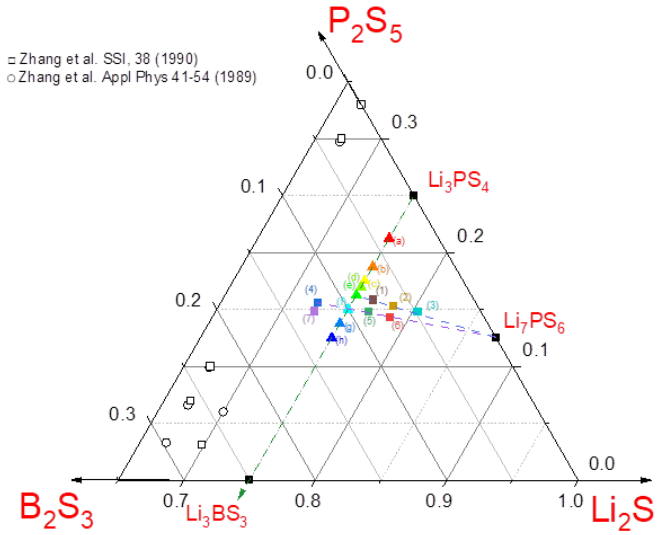

Figure 1. Pseudo-Ternary Li_2S-P_2S_5-B_2S_3 diagram showing studied compounds. Green line corresponds to binary (1-x) Li_3PS_4- x Li_3BS_3, blue line to $Li_3P_{0.85}B_{0.35}S_{3.65}$- Li_7PS_6 binary and purple line to $Li_3P_{0.80}B_{0.40}S_{3.60}$ – Li_7PS_6 binary.

Ref on the ternary diagram	*x in $Li_3P_{1-x}B_xS_{4-x}$*	*Composition*	*Ionic conductivity (mS/cm) (25°C)*	*Activation energy (eV)*
		Binary Li_3PS_4-Li_3BS_3		
(a)	*0.15*	*$Li_3P_{0.85}B_{0.15}S_{3.85}$*	*0.021*	*0.54*
(b)	*0.25*	*$Li_3P_{0.75}B_{0.25}S_{3.75}$*	*0.025*	*0.52*
(c)	*0.3*	*$Li_3P_{0.7}B_{0.3}S_{3.7}$*	*N/A*	*N/A*
(d)	*0.32*	*$Li_3P_{0.68}B_{0.32}S_{3.68}$*	*0.068*	*0.51*
(e)	*0.35*	*$Li_3P_{0.65}B_{0.35}S_{3.65}$*	*0.104*	*0.50*
(f)	*0.4*	*$Li_3P_{0.6}B_{0.4}S_{3.6}$*	*0.11*	*0.57*
(g)	*0.45*	*$Li_3P_{0.55}B_{0.45}S_{3.55}$*	*0.086*	*0.56*
(h)	*0.5*	*$Li_3P_{0.5}B_{0.5}S_{3.5}$*	*N/A*	*N/A*
	1	*Li_3BS_3*		
		Ternary Li_2S-P_2S_5-B_2S_3		
(1)		*$Li_3P_{0.62}B_{0.2}S_{3.5}$*	*0.012*	*0.65*
(2)		*$Li_{3P0.58}B_{0.24}S_{3.33}$*	*0.097*	*0.74*
(3)		*$Li_3P_{0.55}B_{0.18}S_{3.16}$*	*0.011*	*0.9*
(4)		*$Li_3P_{0.64}B_{0.49}S_{3.86}$*	*0.043*	*0.58*
(5)		*$Li_3P_{0.57}B_{0.33}S_{3.44}$*	*0.024*	*0.56*
(6)		*$Li_3P_{0.54}B_{0.27}S_{3.27}$*	*0.020*	*0.57*
(7)		*$Li_3P_{0.61}B_{0.52}S_{3.81}$*	*N/A*	*N/A*

Table 1. Compositions, ionic conductivity at 25°C and corresponding activation energy values for all the compositions studied in Li_2S-P_2S_5-B_2S_3 diagram.

The prepared samples show some impurity phases, therefore, the actual chemical composition may be differing from the nominal chemical composition. Since we were not able to quantify the content of the impurity phase, therefore, for simplicity, we have used nominal chemical compositions of prepared materials in the paper.

In the binary system, the best performing sample was obtained for x= 0.35 i.e. $Li_3P_{0.65}B_{0.35}S_{3.65}$ (see ‡ for synthesis protocol). As shown in the XRD pattern § of Figure 2, The LGPS-type phase started to be visible once a small amount of boron is added to the composition as shown by the XRD peaks at 11.6°, 13.4°, 19.1°, and 22.4° at x = 0.15 in Figure 2 (a). However, many impurities phases like β-Li_3PS_4, γ-Li_3PS_4, and Li_7PS_6 are also visible. As more boron was added to the composition, the purity of LGPS phase improved and reached the maximum purity of the composition at x = 0.35 in the binary system. Further addition of boron beyond x= 0.35, leads to the appearance of a small peak of the Li_3BS_3 phase at 20.3° for x = 0.45. In this Li_3PS_4-Li_3BS_3 domain, we could not achieve a pure LGPS-type phase. Therefore, we further expanded our research to the Li_2S-B_2S_3-P_2S_5 ternary diagram. To differentiate the samples from binary domain, all the samples synthesized in the ternary system are denoted by numbers 1, 2, 3… as given in table 1 with the corresponding targeted composition. According to XRD patterns, the samples with higher purity of Li_3PS_4-Li_3BS_3 binary were at x= 0.35 and x= 0.4. Therefore, it was decided to investigate around these compositions in the Li_2S-B_2S_3-P_2S_5 ternary diagram also. First, we have explored the compositions between $Li_3P_{0.65}B_{0.35}S_{3.65}$ (x=0.35) and Li_7PS_6 to remove the Li_3PS_4 impurity. This binary domain is represented by a blue line as shown in Figure 1. Then, it was repeated for x=0.4, however, in both cases, we observed Li_7PS_6 as an impurity phase. We have also

explored the compositions beyond Li_7PS_6 as shown by the compositions number (4) and (7).

Despite our all efforts, we were not able to obtain a pure phase in this domain also. However, we succeeded to remove β-Li_3PS_4 impurity phase. But for both explored lines i.e. x =0.35 – Li_7PS_6 (Figure 2b) and x =0.4 – Li_7PS_6 (Figure 2c), we observed the Li_7PS_6 phase in both low-temperature and high-temperature polymorphs[18]. The identification of both polymorphs is complicated as they are just characterized by splitting of principal peaks and the crystallinity of our compound still low as shown by the broad peaks. As we go close to the Li_7PS_6 composition, we observe a higher content of Li_7PS_6 phase in the composition. Also, we can confirm that the composition (3) is close to the end of the stability domain of the LGPS-type phase as the principal observed phase is Li_7PS_6. For compositions (4) and (7), we have not observed Li_7PS_6 phase but the β-Li_3PS_4 phase remained visible. The best sample of this series is $Li_3P_{0.58}B_{0.24}S_{3.33}$ (5) as it shows the lowest amount of impurity.

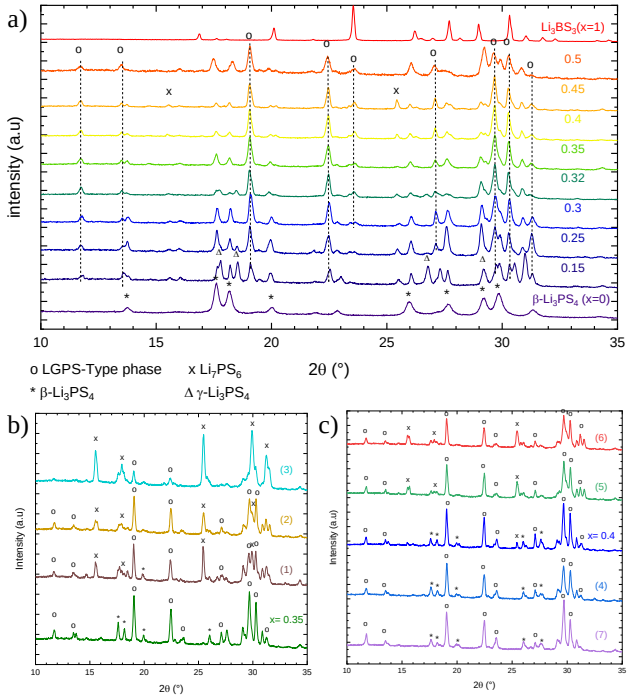

Figure 2. XRD patterns obtained after the synthesis of the ternary Li_2S-P_2S_5-B_2S_3: comparison of synthesis on (a) binary Li_3PS_4-Li_3BS_3 (green line) (b) $Li_3P_{1-x}B_xS_{4-x}$ with x=0.35-Li_7PS_6 binary (blue line) and (c) $Li_3P_{1-x}BxS_{4-x}$ with x= 0.4 - Li_7PS_6 binary (purple line).

A Le-Bail refinement of the compound $Li_3P_{0.65}B_{0.35}S_{3.65}$ (x=0.35) was performed to get some structural information as shown in Figure 3. The space group $P4_2nmc$ has been confirmed by the refinement and the calculated lattice parameters are a = 9.333(2) Å and c = 13.325(8) Å with a volume of 1073 Å^3. Surprisingly, the obtained volume is higher than the lattice volume of $Li_{10}GeP_2S_{12}$ (i.e., 959 Å3)[19]. Since, the ionic radius of boron (0.25 for B^{3+} in coordination IV) is smaller than germanium (0.53 Å for Ge^{4+} in coordination IV))[20], therefore, lattice volume should also be lower. Despite our efforts, we were unable to get the positions of the atoms by ab-initio resolution, as the material is very sensitive to moisture and reactive to beam light. We have also tried an unsuccessful attempt to get TEM resolution. Therefore, advanced structural characterizations like synchrotron or neutron should be done to resolve the structure of the obtained material.

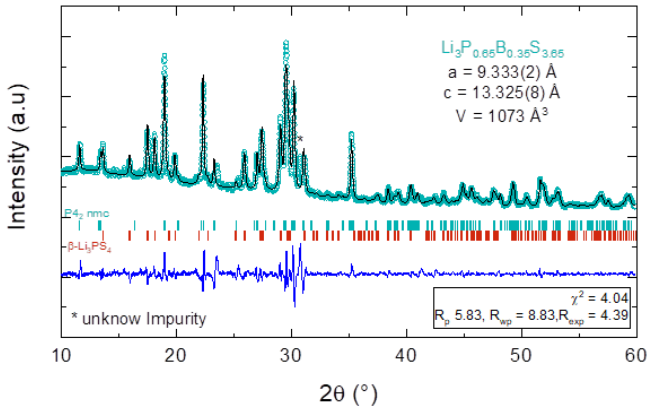

Figure 3. Le-Bail refinement of synthesized compound $Li_3P_{0.65}B_{0.35}S_{3.65}$ composed with a LGPS-type phase and β-Li_3PS_4. An unidentified peak is marked with *.

Despite the presence of Li_3PS_4 impurity, we have studied the electrochemical properties of $Li_3P_{0.6}B_{0.4}S_{3.6}$ compound. Nyquist diagrams [§§] obtained from the material $Li_3P_{0.6}B_{0.4}S_{3.6}$ are shown in Figure S2(a). For the lowest temperature, the Nyquist plots can be summarized in two half-circles and a spike. The equivalent circuit for this situation consists a succession of resistance and a constant phase element (CPE) in parallel, with all being in series with a CPE. The capacity of the CPE can be estimated with the Brug formula[21] (Figure S2b). In the case of the lowest temperature, we used two CPEs parallel to two resistances followed by a CPE, whereas, for the higher temperature, a simple CPE parallel to a resistance followed by a CPE are used (Table S1). The capacity calculated for the first and second CPE is about 10^{-10} F and 10^{-9} F, respectively. Following this value, the first circle can be attributed to the bulk conductivity and the second circle to the grain boundary conductivity[22]. The total conductivity is obtained by overall value of both resistances. As the temperature increases, only one-half circle remains visible as the resistance of the high-frequency half-circle became lower. The plot is therefore fitted with an equivalent circuit with only one parallel CPE and resistance.

As shown in the Arrhenius plot (Figure S3), all the samples follow a linear tendency, which confirms that we are dealing with a thermally activated mechanism. The activation energy of $Li_3P_{0.6}B_{0.4}S_{3.6}$ compound obtained from Arrhenius law is about 0.58 eV (51 kJ/mol). The value of activation energy is higher than the one obtained for LGPS-type ionic conductors (0.31 eV i.e. 30 kJ/mol)[23,24]. As our material is not completely sintered and having impurity phases, it can be suggested that the activation energy is increased by none negligible amount of defects in the material. Although, the Nyquist plots show principally the grain boundary dependency, still, we assume that the activation energy of our sample is principally governed by the impurity phases presented in the grain boundary.

Ionic conductivities of these samples are in the range of 10^{-5} to 10^{-4} S/cm at 25°C. To link conductivity with the composition, ionic conductivity at 25°C have been plotted in color contrast inside the ternary diagram as shown in Figure 4. We can clearly see that the ionic property is higher inside the binary Li_3PS_4-Li_3BS_3. As we add boron into the Li_3PS_4 structure, we observe an increment in the ionic conductivity which reaches a maximum value of 1.17 10^{-4} S/cm for the sample $Li_3P_{0.6}B_{0.4}S_{3.6}$ (x = 0.4). Since, sample $Li_3P_{0.6}B_{0.4}S_{3.6}$ has lower impurity, therefore, it can be concluded that impurity play a major role in the ionic conductivity. The ionic conductivity is close to the value reported by Homma et al.[15] for the highest ionic conductor of their exploration of Li_3PS_4-Li_3BS_4 binary (i.e. 2.2 10^{-4} S/cm). However, the activation energies do not follow exactly the value of

ionic conductivity as shown in Figure S3. Some of the compounds show higher conductivity despite of high activation energy and vice versa. The reduction in activation energy is observed on boron addition into the composition, and lowest value of 0.50 eV (49 kJ/mol) is achieved for the sample $Li_3P_{0.65}B_{0.35}S_{3.65}$ because of the higher purity of the sample. However, ionic conductivity of our compound is 2 orders of magnitude lower in comparison to the LGPS material[24]. The lower conductivity of the materials may lead to higher polarization. However, one should be noticed that our material is neither sintered nor 100% pure, therefore, there is lot of scope to improve the conductivity further.

For compositions outside the Li_3PS_4-Li_3BS_3 binary domain, we have observed a decrease in the total ionic conductivity and an increase in the activation energy. As we already mentioned during XRD analysis, we have observed the formation of Li_7PS_6 impurity when we go closer to this composition. The Li_7PS_6 material is well known for its very low ionic conductivity of 3.5 10^{-8} S/cm at 40 °C for the low temperature polymorph[25]. We can deduce that impurity of Li_7PS_6 is influencing conductivity of our materials.

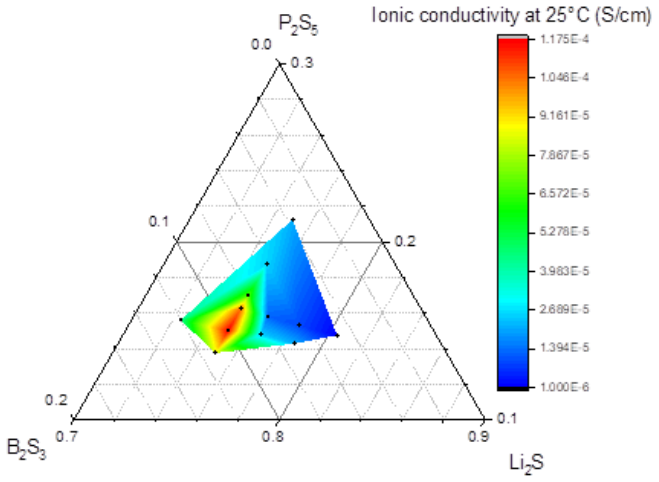

Figure 4. Ionic conductivity at 25°C in function of the Li_2S-P_2S_5-B_2S_3 composition.

To evaluate the electrochemical stability, we investigated $Li_3P_{0.6}B_{0.4}S_{3.6}$ compound by cyclovoltammetry (CV) in reduction and oxidation. Even though, sulfide materials are well known to have a low stability window, we can expect good performance from these materials thanks to the formation of a solid electrolyte interface (SEI)[26]. The material $Li_3P_{0.6}B_{0.4}S_{3.6}$ have been chosen for the CV measurement as it shows the highest ionic conductivity and results are shown in Figure 5. In order to enhance the observed signal, we have mixed some acetylene black with our solid electrolyte to increase the surface area of electronic contact[27]. From the CV cycled in between OCV and 5 V, we can observe a slight increase in the intensity which can be linked to the oxidation of sulfide species into sulfur. Unexpectedly, this electrochemical activity even increases further in the second cycle, which means that the SEI layer formed during the first cycle is not passivating efficiently and further degradation of the electrolyte occurs.

For the cell cycled between OCV and 0 V, we have observed a high intensity peak beginning at 0.9 V. According to the literature, this peak can be associated to the reduction of phosphorus species and the metallic element[28,29]. We can also consider similar process of sulfur reduction in our compound. However, we do not have result to support our claim now. Therefore, it is difficult to find out the exact reason. To get more details about the reactive species, further XPS or XAS analysis need be performed.

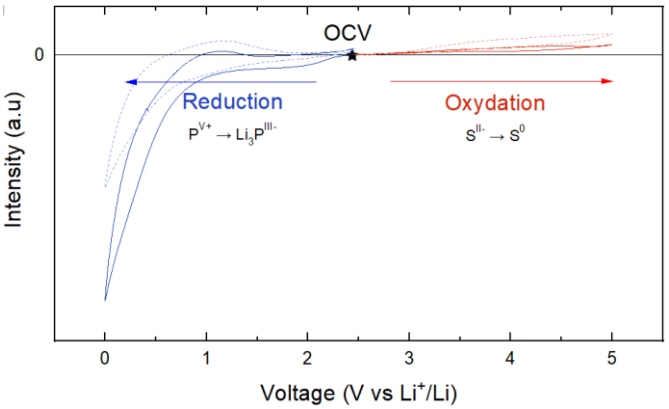

Figure 5. Cyclovoltammetries of the material $Li_3P_{0.6}B_{0.4}S_{3.6}$ between OCV and 0 V (blue curve) and between OCV and 5 V (red curve) at 2 mV/min. The first cycle is shown with solid line and the second cycle with dotted line.

To confirm the formation of a good interface at low potential, the electrochemical stability of the Li-B-P-S based compounds has been tested in symmetric cells [§§§]. We have compared our material with the $Li_{10}GeP_2S_{12}$ compound, which is well known for the instability in reduction[4]. Different current densities have been applied to obtain the maximum value of current before the growth of dendrites. Polarization of our sample remains very stable during cycling when current density is lower than 0.2 mA/cm² (Figure S5). For example, it can be observed an increment in the polarization from 95 mV to 161 mV after 10 cycles at 0.1 mA/cm² (an increase of 70%) for LGPS material as shown in Figure 6(a), whereas, polarization increases from 40 mV to 48 mV (increase of 20% only) for the compound $Li_3P_{0.65}B_{0.35}S_{3.65}$. The difference of polarization increment can be explained by the interface difference in contact with the reducing agent. In the case of LGPS, it is known that the interface is not stable[4,9], which is also visible at beginning of each cycle where a bell shape can be seen due to blocking interface characteristic. The voltage increases until the lithium succeeds to break the bad interface. Whereas, in case of our sample, none of these phenomena is observed showing a better interface formation. At 0.2 mA/cm², we observed the voltage fluctuation response but no clear drop in voltage which generally observes with clear dendrite formation. However, the polarization at 0.2 mA/cm² is lower than twice the polarization at 0.1 mA/cm², confirms the formation of micro dendrite creating partial soft shorts. This result suggests a critical current density at about 0.2 mA/cm².

Similar to ionic conductivity, we have shown polarization of all samples at 0.1 mA/cm² in colour contrast inside the ternary diagram as shown in Figure 6(b). Contrary to ionic conductivity, we observed a minimum polarization for the composition (2) (i.e., $Li_3P_{0.58}B_{0.24}S_{3.33}$). The result claims that ionic conductivity is not the only parameter to focus for the good material. The other materials can form more beneficial interface despite the lower ionic conductivity. As observed during XRD analysis, material $Li_3P_{0.58}B_{0.24}S_{3.33}$ contains Li_7PS_6 impurity phase which seems to be more beneficial than Li_3PS_4 for the formation of a stable interface. We have observed during conductivity measurement that $Li_3P_{0.58}B_{0.24}S_{3.33}$ shows high grain boundary resistance contribution in the EIS spectra. The high grain boundary resistance could be possible due to the presence of secondary phases in the sample, the particle size of the material, and other unknown factors[30]

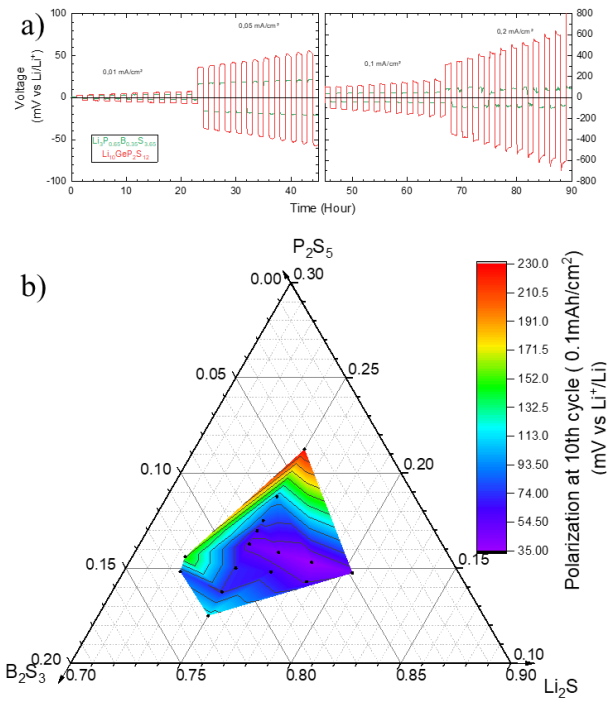

Figure 6. (a) Polarization profile of symmetric cells of compounds $Li_3P_{0.65}B_{0.35}S_{3.65}$ and $Li_{10}GeP_2S_{12}$ at different current density (b) Polarization isoline representation on the ternary Li_2S-B_2S_3-P_2S_5 measured for 0.1 mA/cm² at the 10th cycle. The polarization scale is also shown beside the ternary.

Since, the compound $Li_3P_{0.65}B_{0.35}S_{3.65}$ (LBPS) showed the best electrochemical stability versus lithium in the binary, therefore, this compound also tested in a full cell as a proof of concept and results are compared with $Li_{10}GeP_2S_{12}$ material as shown in Figure 7. The full cells were assembled with $LiNi_{0.8}Co_{0.15}Al_{0.05}O_2$ (NCA) and graphite as a cathode and anode materials, respectively. The positive electrode is prepared from a mixture of NCA and solid electrolyte (LBPS) in the weight ratio of 70:30 to ensure a good ionic percolation[31]. For the negative electrode, a mixture of graphite and electrolyte in the weight ratio of 66:34 is used.

In the Figure 7(a), the first cycle of both compounds is compared. The LBPS compound shows higher polarization during the charge as compared to $Li_{10}GeP_2S_{12}$. At x_{Li} = 0.6, $Li_{10}GeP_2S_{12}$ shows a cell voltage of 3.68 V, whereas the cell voltage of $Li_3P_{0.65}B_{0.35}S_{3.65}$ compound reached at 3.96 V. This leads to a lower charge capacity of 145 mAh/g for the $Li_3P_{0.65}B_{0.35}S_{3.65}$ as compared to 194 mAh/g for the LGPS. The result can relate to the lower conductivity of our compound as compared to LGPS. In addition, full cell performance depends on many factors such as reactivity of solid electrolyte with NCA and graphite, applied current, SEI formation, and mixing at micro level as well as thickness of cathode, solid electrolyte and anode layers. Since, present study does not focus on optimization of these parameters, therefore, it is difficult find the exact reason of higher polarization. However, our material has already shown more stability with lithium as shown in the symmetric cells. Furthermore, we observe better performance during the discharge and less irreversible capacity was observed for our compound. The LGPS compound shows discharge capacity 18 mAh/g only due to non-passivated SEI formation. Whereas, $Li_3P_{0.65}B_{0.35}S_{3.65}$ compound shows a discharge capacity of 72 mAh/g with stable columbic efficiency close to 95% as compared to columbic efficiency of LGPS, which is lower than 90% as shown in Figure 7(b). In case of LGPS solid electrolyte, lithium is consumed in each cycle to form a non-stable SEI which can be seen in the capacity loss. The compound shows only 9.4 mAh/g capacity (i.e. 52% of the initial discharge capacity) after 10 cycles. Whereas, the Li-B-P-S based material $Li_3P_{0.65}B_{0.35}S_{3.65}$ shows capacity retention 70% after 10 cycles due to higher electrochemical stability of the material.

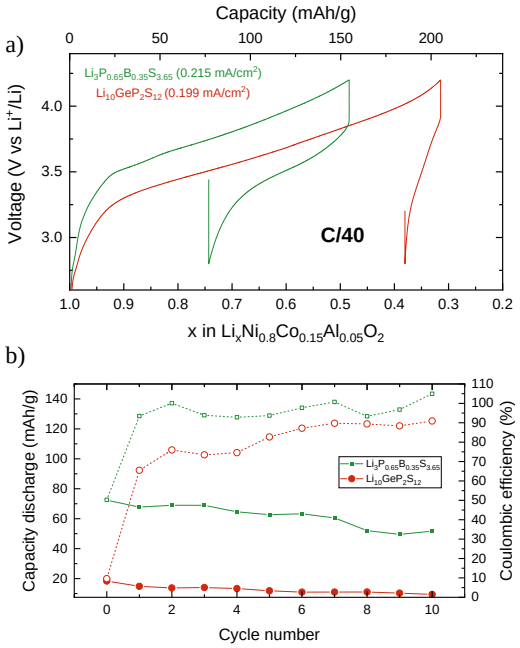

Figure 7. (a) Charge-discharge profiles of full cells NCA:LBPS/LBPS /LBPS:graphite and NCA:LGPS/LGPS/LGPS:graphite at the rate of C/40 (b) Discharge capacities and efficiencies of $Li_3P_{0.65}B_{0.35}S_{3.65}$ and $Li_{10}GeP_2S_{12}$ compounds.

As our compounds are sulfide based, therefore, their stability against ambient moisture has been investigated for safety purpose. During the exposition to the ambient moisture of sulfide based lithium solid electrolytes, a hydrolysis reaction occurs which converts sulfide based compounds into oxides and releases a toxic H_2S gas according to following reaction:

$Li_xMS_y + y\ H_2O \rightarrow Li_xMO_y + y\ H_2S$

The nature of the M atom thermodynamically rules the hydrolysis process as the activation energy of this reaction depends on the energy release during formation of oxide material[32].

Figure 8 shows the amount of H_2S gas released by the compound $Li_3P_{1-x}B_xS_{4-x}$ after exposure to moisture and comparison was done with Li_3BS_3, β- Li_3PS_4 and $Li_{10}GeP_2S_{12}$ compounds §§§§. The family of $Li_3P_{1-x}B_xS_{4-x}$ compounds show very high reactivity with ambient moisture. All the compounds of the binary reach the sensor limit of 33 cm^3/g in less than 20 min, whereas the β- Li_3PS_4 material releases only 0.4 cm^3/g after 20 min. The low stability of $Li_3P_{1-x}B_xS_{4-x}$ compounds can be explained by the boron in the composition. As we can see that Li_3BS_3 is the most reactive compound of the system and by introducing phosphorus inside the compound, air reactivity of Li_3BS_3 is found to be lower. In addition, the β-Li_3PS_4 shows the highest stability in all compounds which means phosphorus compound is very stable against moisture. Also, if we compare the results with $Li_{10}GeP_2S_{12}$ material, we can deduce that the bad stability of boron-based compounds against moisture does not come from the structure as these compounds also have LGPS type structure.

These results are in accordance with the theoretical calculation made by Zhu and al.[32]. By studying the thermodynamic of hydrolysis reaction Li-M-S compound, the study shows the lower stability of boron compared to phosphorus system. In fact, this element shows the lowest stability versus moisture after beryllium.

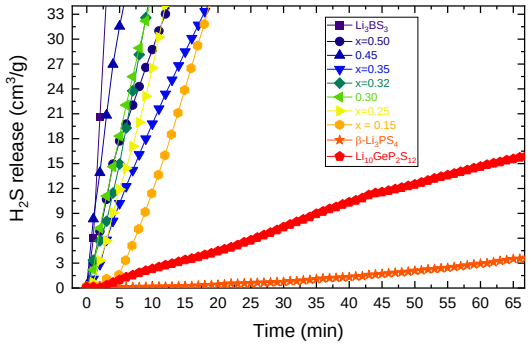

Figure 8. Evolution curve of the H_2S gas generated from $Li_3P_{1-x}B_xS_{4-x}$ compound after exposition to air versus time. Li_3BS_3, β–Li_3PS_4, and $Li_{10}GePS_{12}$ are reported for the sake of comparison.

Conclusions

In the present work, we have explored the Li_3PS_4-Li_3BS_3 binary system. Furthermore, we have also extended our study to the Li_2S-P_2S_5-B_2S_3 ternary domain. Despite our efforts to optimize the synthesis, we could not succeed in obtaining a pure LGPS phase, and the impurity phases such as β–Li_3PS_4 or Li_7PS_6 remained in the final sample. However, despite these impurities, a decent ionic conductivity of 1.17 10^{-4} S/cm is obtained for the sample $Li_3P_{0.6}B_{0.4}S_{3.6}$. Also, we measure very low and stable polarization during cycling in symmetrical cells for this family of compounds which confirms their good compatibility with lithium. In case of the binary Li3PS4-Li3BS3, the compound $Li_3P_{0.65}B_{0.35}S_{0.65}$ shows a significantly lower polarization in the symmetrical cell as compared to LGPS (almost divided by 2: 45 mV at 0.1 mA/cm²). Furthermore, an even better results are observed for the compound $Li_3P_{0.58}P_{0.24}S_{3.33}$ in the ternary domain where a value of 35 mV was observed for the same current density.

The full-cell test confirmed the better stability on the negative side of compounds of LBPS family as compared to $Li_{10}GeP_2S_{12}$. The LBPS retained 51 mAh/g after 10 cycles, whereas, LGPS based cell showed discharge capacity only 9.4 mAh/g. Even though, the capacity delivered by LBPS is lower than the theoretical capacity of NCA cathode but it provides the better compatibility with negative electrode of the battery. However, compounds prepared with boron and sulfur show low stability in the ambient humidity which needs to be addressed before using this family of materials on a larger scale.

Author Contributions

C J. and V.Pra. are at the origin of the scientific project. A.N. performed all the experiments. H. R. and V. Pel. strongly participate to the scientific discussion and the improvement of the manuscript writing.

Conflicts of interest

There are no conflicts to declare.

Acknowledgements

The authors thank to J. Jean, J. Lecourt, S. Gascoin, S. Duffourt and X. Larose for technical help. We gratefully acknowledge the CNRS, the Ministry of Education and Research, Normandy region and SAFT through the contract SAFT-CNRS n°2019-42356 as well the financial support from the French National Research Agency (project Labex STORE-EX, ANR-10-LABX-76-01) and from the Intercarnot Project #252156 "CaKi - Cathode Materials for K-ion Batteries" (Carnot Institutes EPS and CBC).

Notes and references

‡ For the synthesis, classical mechanochemical method followed by annealing in sealed tubes under vacuum was performed [6,33,34]. The precursors Li_2S (Alfa Aesar 99.9%), P_2S_5 (Aldrich 99%), boron powder (Alpha Aesar 98%), germanium powder (Alpha Aesar 99.999%) and sulfur powder (Alpha Aesar 99.5%) were used, and all the chemicals were handled under a high purity argon atmosphere (H_2O<0.1 ppm, O_2<0.1ppm). Precursors were weighed in stoichiometric ratios and ground by planetary milling for 45 h at 370 RPM (FRITSCH, 25 ml ZrO_2 bowls with 4 balls). Bowls were scraped after every 15 hours to peel off powder from the walls. Then, the mixture was pelletized at 160 MPa, placed in a carbon coated sealed quartz tube and annealed at 550°C for 4 hours.

§ For XRD measurement, all the samples were placed in the air sensible sample holder from Rigaku and measured with a Miniflex diffractometer with Bragg-Brentano geometry ($CuK_{\alpha1,2}$ radiation). The refinement of the XRD patterns was carried out using the Rietveld method in Fullprof suite software[35].

§§ For impedance spectroscopy measurement, samples were firstly pelletized with a die of 10 mm under 160 MPa and then pressed at 9 T under isostatic condition. The sample was then polished under dry condition in glove box and gold-plated on both sides by sputter deposition. After this step, the thickness of the sample was about 1.0 mm. The sample was then placed inside the Bio-logic Controlled Environment Sample Holder (CESH). A signal with an amplitude of 50 mV and frequencies between 1 MHz and to 0.1 Hz was applied using a VMP3 from Bio-logic. Temperature was controlled by the Bio-logics Intermediate Temperature System (ITS) between 80°C and -40°C.

§§§ For symmetric cells, 50 mg of solid electrolyte material was pressed at 255 MPa in the cell presented previously[36]. The pressed material resulted in in a pellet of about 600 µm. Then, Li metal (200 µm, Aldrich) was placed both sides of the electrolyte and pressed with the screws of the cells at 2 N.m. For cycling voltammetry, 50 mg of material was pressed at 255 Mpa and a mixture of carbon and solid electrolyte was added one side and pressed at 255 MPa. Similarly, lithium metal was added on the other side of the electrolyte and pressed with screws of the cells at 2 N.m. For the full battery cells, solid electrolyte was mixed with $LiNi_xCo_yAl_zO_2$ (NCA) and graphite in the wt. ratios of (30:70) and (34:66) for positive and negative electrode materials, respectively. For cell assembling, about 40 mg of an electrolyte was pressed at 255 MPa and then negative and positive electrode materials (about 15mg for each) were pressed on each side of the electrolyte at 255 MPa. The calculated loading for the positive electrode was about 38 mg/cm² whereas, surface area of the electrode was 0.38 cm². The pressure was maintained during charge-discharge cycling by the screws of the cell. The applied current was calculated based on the loading of NCA cathode and

C-rate (C/40) was determined according theoretical capacity (1C = 179 mAh/g) of NCA.

§§§§ The amount of H_2S generated from the prepared solid electrolyte samples was measured with a H_2S sensor (Croncow, Gasman) by exposing samples in ambient atmosphere. For the H_2S measurement, about 30±2 mg of pelletized powder was placed inside 4000 cm3 air-tight vessel. To ensure a constant humidity level, 20 mL of H_2O were also placed inside the desiccator. The generated H_2S (in cm^3/g) was calculated from the H_2S concentration inside the vessel by the H_2S sensor in ppm.

1 X. Wu, K. Song, X. Zhang, N. Hu, L. Li, W. Li, L. Zhang and H. Zhang, *Front. Energy Res.*, , DOI:10.3389/fenrg.2019.00065.

2 A. Manthiram, X. Yu and S. Wang, *Nature Reviews Materials*, , DOI:10.1038/natrevmats.2016.103.

3 N. Kamaya, K. Homma, Y. Yamakawa, M. Hirayama, R. Kanno, M. Yonemura, T. Kamiyama, Y. Kato, S. Hama, K. Kawamoto and A. Mitsui, *Nature Materials*, 2011, **10**, 682–686.

4 S. Wenzel, S. Randau, T. Leichtweiß, D. A. Weber, J. Sann, W. G. Zeier and J. Janek, *Chemistry of Materials*, 2016, **28**, 2400–2407.

5 S. Hori, K. Suzuki, M. Hirayama, Y. Kato, T. Saito, M. Yonemura and R. Kanno, *Faraday Discuss.*, 2015, **176**, 83–94.

6 Y. Sun, K. Suzuki, S. Hori, M. Hirayama and R. Kanno, *Chem. Mater.*, 2017, **29**, 5858–5864.

7 P. Bron, S. Johansson, K. Zick, J. Schmedt auf der Günne, S. Dehnen and B. Roling, *J. Am. Chem. Soc.*, 2013, **135**, 15694–15697.

8 P. Bron, S. Dehnen and B. Roling, *Journal of Power Sources*, 2016, **329**, 530–535.

9 P. Bron, B. Roling and S. Dehnen, *Journal of Power Sources*, 2017, **352**, 127–134.

10 Y. Kato, S. Hori, T. Saito, K. Suzuki, M. Hirayama, A. Mitsui, M. Yonemura, H. Iba and R. Kanno, *Nature Energy*, 2016, **1**, 16030.

11 Z. Zhang and J. H. Kennedy, *Solid State Ionics*, 1990, **38**, 217–224.

12 K. Kaup, J. D. Bazak, S. H. Vajargah, X. Wu, J. Kulisch, G. R. Goward and L. F. Nazar, *Advanced Energy Materials*, 2020, **10**, 1902783.

13 P. Vinatier, P. Gravereau, M. Ménétrier, L. Trut and A. Levasseur, *Acta Crystallographica Section C*, 1994, **50**, 1180–1183.

14 K. Kaup, A. Assoud, J. Liu and L. F. Nazar, *Angewandte Chemie*, 2021, **133**, 7051–7056.

15 K. Homma, T. Yamamoto, S. Watanabe and T. Tanaka, *ECS Trans.*, 2013, **50**, 307.

16 Z. Zhang, J. H. Kennedy, J. Thompson, S. Anderson, D. A. Lathrop and H. Eckert, *Appl. Phys. A*, 1989, **49**, 41–54.

17 R. Kanno and M. Murayama, *J. Electrochem. Soc.*, 2001, **148**, A742–A746.

18 S. T. Kong, Ö. Gün, B. Koch, H. J. Deiseroth, H. Eckert and C. Reiner, *Chemistry – A European Journal*, 2010, **16**, 5138–5147.

19 O. Kwon, M. Hirayama, K. Suzuki, Y. Kato, T. Saito, M. Yonemura, T. Kamiyama and R. Kanno, *J. Mater. Chem. A*, 2014, **3**, 438–446.

20 R. D. Shannon, *Acta Cryst A*, 1976, **32**, 751–767.

21 G. J. Brug, A. L. G. van den Eeden, M. Sluyters-Rehbach and J. H. Sluyters, *Journal of Electroanalytical Chemistry and Interfacial Electrochemistry*, 1984, **176**, 275–295.

22 J. T. S. Irvine, D. C. Sinclair and A. R. West, *Adv. Mater.*, 1990, **2**, 132–138.

23 Y. Gao, N. Li, Y. Wu, W. Yang and S. Bo, *Adv. Energy Mater.*, 2021, **11**, 2100325.

24 Y. Kato, S. Hori and R. Kanno, *Adv. Energy Mater.*, 2020, 2002153.

25 H.-J. Deiseroth, J. Maier, K. Weichert, V. Nickel, S.-T. Kong and C. Reiner, *Zeitschrift für anorganische und allgemeine Chemie*, 2011, **637**, 1287–1294.

26 A. Sakuda, A. Hayashi and M. Tatsumisago, *Chem. Mater.*, 2010, **22**, 949–956.

27 G. F. Dewald, S. Ohno, M. A. Kraft, R. Koerver, P. Till, N. M. Vargas-Barbosa, J. Janek and W. G. Zeier, *Chem. Mater.*, 2019, **31**, 8328–8337.

28 T. Swamy, X. Chen and Y.-M. Chiang, *Chem. Mater.*, 2019, **31**, 707–713.

29 D. H. S. Tan, E. A. Wu, H. Nguyen, Z. Chen, M. A. T. Marple, J.-M. Doux, X. Wang, H. Yang, A. Banerjee and Y. S. Meng, *ACS Energy Lett.*, 2019, **4**, 2418–2427.

30 E. Milan and M. Pasta, *Mater. Futures*, 2022, **2**, 013501.

31 W. Zhang, D. A. Weber, H. Weigand, T. Arlt, I. Manke, D. Schröder, R. Koerver, T. Leichtweiss, P. Hartmann, W. G. Zeier and J. Janek, *ACS Appl. Mater. Interfaces*, 2017, **9**, 17835–17845.

32 Y. Zhu and Y. Mo, *Angewandte Chemie International Edition*, 2020, **59**, 17472–17476.

33 Y. Kato, R. Saito, M. Sakano, A. Mitsui, M. Hirayama and R. Kanno, *Journal of Power Sources*, 2014, **271**, 60–64.

34 K.-H. Kim and S. W. Martin, *Chemistry of Materials*, 2019, **31**, 3984–3991.

35 T. Roisnel and J. Rodríquez-Carvajal, *Materials Science Forum*, 2001, **378–381**, 118–123.

36 X. Wu, M. El Kazzi and C. Villevieille, *Journal of Electroceramics*, 2017, **38**, 207–214.